Crack Width Evaluation of Steel Reinforced FRCC members

（鉄筋補強 FRCC 部材のひび割れ幅評価）

Daiki Sunaga

（Master's Program in Engineering Mechanics and Energy）

Advised by Toshiyuki Kanakubo

Submitted to the Graduate School of
Systems and Information Engineering
in Partial Fulfillment of the Requirements
for the Degree of Master of Engineering
at the
University of Tsukuba

March 2021

Abstract

Fiber-reinforced cementitious composite (FRCC) is cementitious material reinforced with short discrete fibers showing ductile behavior of composite, especially in tensile and bending field. The main advantage of FRCC lies on the controlling of crack width by bridging effect of fibers across crack. FRCC is generally utilized with steel reinforcing rebars in actual structures similarly as conventional concrete structures, hence, it is essential to evaluate crack width considering both fiber bridging effect and bond interaction between FRCC and rebar.

This study aims to evaluate crack width in steel-reinforced FRCC members for the practical structures' design. The theoretical calculation formula to predict crack width in steel-reinforced FRCC was led by solving the force equilibrium and compatibility conditions between FRCC and reinforcing bar considering bond interaction, fiber bridging effect and condition of crack occurrence. The steel strain – crack width relationship was given by a simple formula using bond constitutive law and fiber bridging law in addition to the material parameters of FRCC and rebar.

Uniaxial tension test was conducted for steel-reinforced FRCC prism specimens using aramid and PVA fibers to measure crack width experimentally. The test parameters were cross-sectional size of prism, fiber types and fiber volume fraction of FRCC. After that, theoretical curves were calculated by using the proposed formula and compared with the test results. The theoretical curves showed a good adaptability to evaluate crack width in each test parameter. According to the evaluation results using theoretical curves, crack width was smaller in PVA-FRCC by comparing with aramid-FRCC.

Parametric study of theoretical curves was conducted using the models of bridging laws for 4 types of fibers. In addition to aramid and PVA fibers used in the uniaxial tension test, PP and steel fibers were also subjected to the calculation. The crack width at the same steel strain became smaller in the order of PP, aramid, PVA and steel fiber, which was the same order that the initial slope of the bridging laws became larger.

Crack Width Evaluation of Steel Reinforced FRCC members

（鉄筋補強 FRCC 部材のひび割れ幅評価）

CONTENTS

List of Figures

List of Tables

Chapter 1 Introduction

1.1 Research Background

1.1.1 Fiber-Reinforced Cementitious Composites (FRCC)

Fiber-reinforced cementitious composite (FRCC) is cementitious material mixed with short discrete fibers into cement matrix to improve brittle behavior of composites especially in tensile and bending field. FRCC shows high ductility because of fiber bridging through cracks and control the crack opening as shown in **Figure 1.1**(a). FRCC has been also expected to bring high durability to reinforced concrete structures by its small opening cracks that prohibit the penetrations of aggressive attacks to deteriorate the internal reinforcing rebars and FRCC itself.

In past several decades, various types of FRCCs have been introduced and studied by lots of researchers. Steel fibers or polymeric fibers such as polyethylene (PE), polyvinyl alcohol (PVA), and polypropylene (PP) fibers have been utilized in FRCCs. While steel fiber-reinforced concrete (SFRC) commonly shows tension-softening behavior after initial cracking, FRCCs which are recently developed and studied show much higher ductility. FRCC showing a deflection hardening behavior under bending condition is defined as ductile fiber-reinforced cementitious composites (DFRCC) [1], while FRCC showing pseudo-strain hardening behavior under the uniaxial tension is defined as strain hardening cementitious composites (SHCC) [2]. In addition, DFRCC and SHCC show multiple cracking behavior as shown in **Figure 1.1**(b). The high ductility of these materials is achieved by the bridging effect of individual fibers in the matrix. In DFRCC and SHCC, polymeric fibers are commonly used rather than steel fiber. Engineered cementitious composites (ECC) [3], a class of cementitious materials typically reinforced with PE or PVA fibers, are one of the examples of SHCC materials showing high tensile strain hardening ability. Actual applications have been reported using them for beams, walls, decks and slabs, tunnel linings, concrete substrate retrofitting materials, etc. It has been expected to expand the use of these FRCCs with additional values for resilient and sustainable structures.

(a)

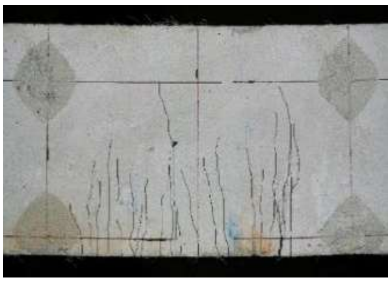

(b)

Figure 1.1 FRCC under bending condition:
(a) Crack bridging through crack; (b) Multiple cracking behavior

1.1.2 Crack Width Evaluation of FRCC (Fiber Bridging Law)

It's no exaggeration to say that the advantage of FRCC lies on the controlling of crack width by bridging effect of fibers across the crack. The tensile stress - crack width relationships (hereafter, called bridging law) can feature the crack width and crack opening behavior of FRCC itself and have been studied by many researchers. In general, bridging law of FRCC can be directly obtained from a uniaxial tension test [4-5], or alternatively, indirectly from a prism bending test [6]. However, in SHCC, it is difficult to measure the crack opening of single crack because of the multiple cracking behavior. To solve this problem, Pereira et al. have proposed the unique testing method using 0.5mm thick notched specimen [7] and Yu et al. have proposed the high-precision measuring method of crack opening using Digital Image Processing [8].

On the other hand, the micromechanical modeling of bridging law of steel and PP fiber-reinforced concrete was first introduced by Li et al. [9]. Tensile stress can be given by the function of crack opening that is featured by the slip-out behavior of the individual fibers considering the effect of the inclined angle and probability density function for fiber dispersion and orientation. Especially in SFRC, bridging law has been studied theoretically by some researchers (e.g. [10]). Furthermore, Yang et al. have updated the micromechanical bridging law model for PVA-ECC by including strain-hardening behavior [11]. Kanakubo et al. have also studied bridging law for PVA-FRCC [12] and aramid-FRCC [13]. The both calculated bridging laws showed good agreements with the results of uniaxial tension test. In addition, the calculated bridging law of PVA-FRCC has been expressed by tri-linear model by Ozu et al. [14]. The characteristics points of the model have been given by the function of fiber orientation intensity. Since the bridging performance is varied by the fiber orientation, the model makes it easier to evaluate crack width in various types of FRCC members.

1.1.3 Crack Width Evaluation of Steel Reinforced FRCC members

FRCC is generally utilized with steel reinforcing rebars in actual structures similarly as conventional concrete structures. As well known, crack width in conventional concrete structures is affected not only by the characteristics of concrete but also by reinforcement ratio and interaction between concrete and rebars. For conventional concrete, Kanakubo et al. have proposed a crack width prediction method led by calculation of bond interactions [15]. The crack width is expressed by a simple function of dimensions of concrete prism and rebar, bond stiffness, tensile strength of concrete, and strain of rebar.

For FRCC, in fact, some researchers have conducted uniaxial tension test of steel-reinforced FRCC prisms and evaluated cracking behavior [16-18]. Although the crack width of FRCC itself can be obtained through bridging law, it is considered that crack width in steel-reinforced FRCC member is also affected by the interaction between rebars as shown in **Figure 1.2**. Some researchers have studied theoretical calculations of crack width in FRCC with conventional reinforcement considering both the interaction of steel deformed rebar and fiber bridging effect at cracks [19-21]. Sunaga et al. have also conducted bond analysis for steel-reinforced FRCC prism considering fiber bridging effect and evaluated crack opening behavior [22]. However, these methodologies are complicated and require convergence calculations or numerical analyses to solve. It is quite convenience in the practical structures' design to calculate crack width by a simple formula in which the crack width is expressed using the stress or strain of rebars.

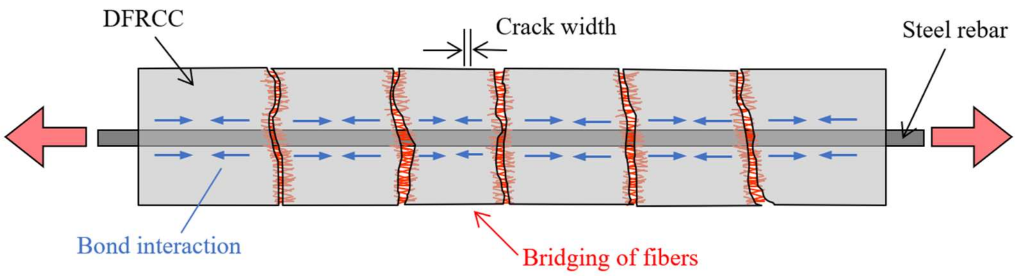

Figure 1.2 Schematic drawing of uniaxial tension test for steel-reinforced FRCC

1.2 Research Objective

The main objective of this study is to evaluate crack width in steel-reinforced FRCC members for the practical structures' design. To achieve this goal, a simple evaluation method of crack width in steel-reinforced FRCC is derived by theoretical calculation of bond interactions between steel deformed rebar and FRCC, considering bridging effect of fibers at crack. Uniaxial tension test is conducted for steel-reinforced FRCC prism specimens with slits and crack width is measured experimentally to verify the adaptability of proposed evaluation method.

Chapter 2 Theoretical Solution of Crack Width Prediction

2.1 Introduction

In the previous study [15], theoretical solution of crack width in steel-reinforced concrete member have been obtained based on the equilibrium and compatibility conditions considering the bond interaction between concrete and rebar. The crack width is given by the function of the strain of rebar. In this chapter, same theoretical procedure is also conducted in streel reinforced FRCC member involving the bridging effect of fibers at crack.

2.2 Theoretical Solution of Crack Width Prediction

The relationship between strain of reinforcing bar and crack width is obtained from the equilibrium of axial forces and compatibility conditions in infinitesimal element of reinforced FRCC.

Figure 2.1 shows the infinitesimal element of reinforced FRCC under tensile condition. Where, dx is length of the infinitesimal element, P_{sx} is tensile load of rebar, dP_{sx} is increment of tensile load of rebar in dx, τ_x is bond stress, s_x is slip and ds_x is increment of slip in dx. Eq.(1) gives the definition of bond stress which is obtained from the force equilibrium of rebar in axial direction.

$$\frac{dP_{sx}}{dx} = \tau_x \cdot \varphi_s \tag{1}$$

where φ_s is perimeter of rebar. Assuming that the rebar behaves in elastic manner, tensile force of rebar is expressed by strain as Eq.(2)

$$\frac{d\varepsilon_{sx}}{dx} = \frac{\varphi_s}{E_s A_s} \cdot \tau_x \tag{2}$$

where, ε_{sx} is strain of rebar, E_s is elastic modulus of rebar, and A_s is cross-sectional area of rebar. Since the slip is defined as difference of deformation between rebar and surrounding FRCC, Eq.(3) is obtained from compatibility condition in the infinitesimal element.

$$\frac{ds_x}{dx} = \varepsilon_{sx} - \varepsilon_{cx} \tag{3}$$

where ε_{cx} is strain of FRCC.

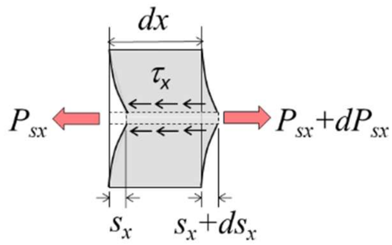

Figure 2.1 Infinitesimal element of reinforced FRCC under tensile condition

A reinforced FRCC prism which is subjected to uniaxial tensile load is shown in **Figure 2.2**. Cracks occur in the prism by increasing the tensile load at loaded end, $P_{s(LOAD)}$. Uncracked region between two cracks is focused and x-axis is defined in axial direction of the prism as the origin positions at the center of the uncracked region (x = 0). The half-length of the uncracked region is defined as l so that the crack locates at $x = l$. P_{sx} and P_{cx} represent tensile forces of rebar and that of FRCC at arbitrary position in the uncracked region, x, respectively. At the crack in reinforced FRCC, tensile force is transferred not only by the rebar, P_{sl}, but also by the bridging of fibers, P_{br}. Eq.(4) gives the equilibrium condition of axial forces. Eq.(4) leads Eq.(5) assuming that the rebar and FRCC in the uncracked region remains in elastic.

$$P_{sx} + P_{cx} = P_{sl} + P_{br} \left(= P_{s(LOAD)}\right) \tag{4}$$

$$np\varepsilon_{sx} + \varepsilon_{cx} = np\varepsilon_{sl} + \frac{1}{E_c}\sigma_{br} \left(= np\varepsilon_{s(LOAD)}\right) \tag{5}$$

where,

σ_{br} : fiber bridging stress at crack (=P_{br}/A_c),

ε_{sl} : strain of rebar at crack,

$\varepsilon_{s(LOAD)}$: strain of rebar at loaded end,

n : ratio of elastic modulus (=E_s/E_c),

p : reinforcement ratio (=A_s/A_c),

E_s : elastic modulus of rebar,

E_c : elastic modulus of FRCC,

A_s : cross-sectional area of rebar,

A_c : cross-sectional area of FRCC.

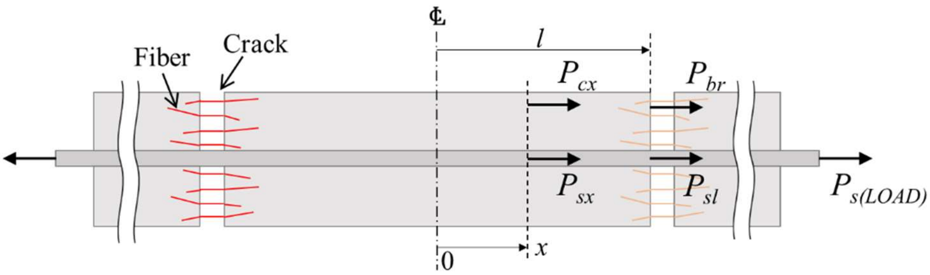

Figure 2.2 Cracked reinforced FRCC prism in tension

Substituting Eq.(5) for Eq.(3), Eq.(6) is obtained. Eq.(2) and Eq.(6) lead Eq.(7).

$$\frac{ds_x}{dx} = (1 + np) \cdot \varepsilon_{sx} - np \cdot \varepsilon_{sl} - \frac{1}{E_c}\sigma_{br} \tag{6}$$

$$\frac{d\varepsilon_{sx}}{ds_x} = \frac{\varphi_s}{E_s A_s} \cdot \frac{\tau_x}{(1 + np) \cdot \varepsilon_{sx} - np \cdot \varepsilon_{sl} - \frac{1}{E_c}\sigma_{br}} \tag{7}$$

Integration of Eq.(7) from the center (x = 0) to crack position (x = l) is expressed by Eq.(8).

$$\int_{\varepsilon_{s0}}^{\varepsilon_{sl}} \{(1 + np) \cdot \varepsilon_{sx} - np \cdot \varepsilon_{sl} - \frac{1}{E_c}\sigma_{br}\} d\varepsilon_{sx} = \int_{s_0}^{s_l} \frac{\varphi_s}{E_s A_s} \cdot \tau_x \, ds_x \tag{8}$$

where,

ε_{s0} : strain of rebar at x = 0,

s_0 : slip at x = 0,

s_l : slip at x = l.

Slip at x = 0, i.e., relative displacement between rebar and FRCC at the center of uncracked region can be assumed to be zero (s_0 = 0) because of the symmetric condition. Integral calculus of Eq.(8) gives Eq.(9).

$$\frac{1 + np}{2}\left(\varepsilon_{sl}^{\,2} - \varepsilon_{s0}^{\,2}\right) - \left(np \cdot \varepsilon_{sl} + \frac{1}{E_c}\sigma_{br}\right)(\varepsilon_{sl} - \varepsilon_{s0}) = \frac{\varphi_s}{E_s A_s}\int_0^{s_l} \tau_x \, ds_x \tag{9}$$

Eq.(9) gives the fundamental relationships between strains of rebar (ε_{s0} and ε_{sl}) and slip at crack (s_l). To achieve the goal of this study, it is convenience that the slip at crack can be expressed only by the strain of rebar at crack. An additional condition is introduced to eliminate the term of ε_{s0}.

Tensile stress in FRCC becomes the largest at the center (x = 0) in uncracked region due to transmitted stress from rebar via bond stress. When tensile force of rebar increases, a new crack in FRCC is generated at the center of uncracked region resulting that the uncracked region is separated into two parts. The slip at crack which locates the end of uncracked region shows largest value just at the generation of the new crack. This condition means that the slip at crack is maximized when tensile stress in FRCC at the center reaches its cracking strength. This condition leads Eq.(10), where σ_{cr} is cracking strength of FRCC. Eq.(10) expresses that tensile strength at cracking in FRCC has the equilibrium with the bridging force at crack and the increment force by bond stress.

$$\sigma_{cr}A_c = \varphi_s \cdot \int_0^l \tau_x \, dx + \sigma_{br}A_c \tag{10}$$

Substituting Eq.(2) for Eq.(10), Eq.(11) is derived. Eq.(11) is calculated as Eq.(12).

$$\sigma_{cr}A_c = E_sA_s \int_0^l \frac{d\varepsilon_{sx}}{dx} dx + \sigma_{br}A_c = E_sA_s \int_{\varepsilon_{s0}}^{\varepsilon_{sl}} d\varepsilon_{sx} + \sigma_{br}A_c \tag{11}$$

$$\sigma_{cr}A_c = E_sA_s \cdot (\varepsilon_{sl} - \varepsilon_{s0}) + \sigma_{br}A_c \tag{12}$$

Substituting Eq.(12) for Eq.(9), strain of rebar at crack position, ε_{sl}, is given by Eq.(13).

$$\varepsilon_{sl} = \frac{\varphi_s}{A_c(\sigma_{cr} - \sigma_{br})} \int_0^{s_l} \tau_x \, ds_x + \frac{1}{E_c}\sigma_{br} + \frac{1 + np}{2npE_c}(\sigma_{cr} - \sigma_{br}) \tag{13}$$

Eq.(13) expresses the relationship between strain of rebar and slip at crack position when a new crack generates. Since crack width of FRCC can be considered to involve the slips from the both sides of uncracked regions, it can be assumed that the slip at the crack position gives half of crack width. So, Eq.(13) gives the relationship between strain of rebar at crack position and crack width which has the possibility to become the maximum.

Eq.(13) is adaptable for the materials in elastic manner in tension and with any relations between bond stress and slip. However, bond stress should be given by function of slip to solve Eq.(13). In this study, since the target range of slip (half of crack width) is enough small, bond stress versus slip relations is assumed to be given by elastic model. This assumption also helps to obtain mathematical solution by easy form for the practical use. The model is defined by bond stiffness, k_{bo}, as given in Eq.(14).

$$\tau_x = k_{bo} \cdot s_x \tag{14}$$

Using Eq.(14), integral calculus for bond stress in Eq.(13) is derived as Eq.(15).

$$\int_0^{s_l} \tau_x \, ds_x = \frac{1}{2}k_{bo} \cdot {s_{sl}}^2 \tag{15}$$

Substituting Eq.(15) for Eq.(13), and assuming that crack width, w_{cr}, is equal to two times slip at crack position, Eq.(16) is derived.

$$\varepsilon_{sl} = \frac{k_{bo}\varphi_s}{8A_c(\sigma_{cr} - \sigma_{br})}{w_{cr}}^2 + \frac{1}{E_c}\sigma_{br} + \frac{1 + np}{2npE_c}(\sigma_{cr} - \sigma_{br}) \tag{16}$$

It can be considered that fiber bridging stress, σ_{br}, has also relations with crack width. The crack bridging stress of fibers in FRCC, σ_{br}, is given by the fiber bridging law, i.e., the function of crack width, w_{cr}. Therefore, Eq. (16) can be expressed as follows.

$$\varepsilon_{sl} = \frac{k_{bo}\varphi_s}{8A_c\{\sigma_{cr} - \sigma_{br}(w_{cr})\}} {w_{cr}}^2 + \frac{1}{E_c}\sigma_{br}(w_{cr}) + \frac{1+np}{2npE_c}\{\sigma_{cr} - \sigma_{br}(w_{cr})\} \tag{17}$$

Eq.(17) gives the relationship between strain of rebar at crack position and crack width when a new crack generates at the center of uncracked region. The crack width given by this relationship is corresponding to the maximum value for the following reasons.

Figure 2.3 shows the schematic drawings of rebar strain – crack width relationship expressed by Eq.(17). The dotted lines in **Figure 2.3** shows the examples of crack opening behavior of a certain crack. When the crack width reaches to the theoretical value with increasing of steel strain, new crack generates at the center of uncracked region. That is because this formula is led by using condition that tensile stress at the center of uncracked FRCC reaches to the cracking strength. This phenomenon causes the increasing of the number of cracks, hence, the crack width of each crack decreases because crack width is given as total deformation of specimen divided by the number of cracks. For this reason, crack opening of a certain crack does not exceed the theoretical value. Therefore, it can be said that this formula gives the possible maximum crack width at arbitrary strain of rebar. As the feature of this formula, crack spacing (=two times bond length) is not required for the calculation.

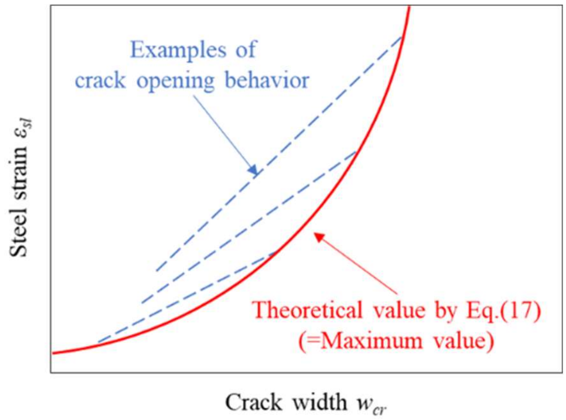

Figure 2.3 Rebar strain – crack width relationship expressed by Eq.(17)

Here, to compare the calculations by Eq.(17) with the test results, equilibrium of the axial force between crack position and loaded end is considered as previously shown in **Figure 2.2**. As seen in Eq.(18), the summation of tensile force of steel rebar at crack position, P_{sl}, and fiber bridging force, P_{br}, is equal to the tensile force of steel rebar at loaded end, $P_{s(LOAD)}$. Note that, $P_{s(LOAD)}$ is corresponding to the test load of uniaxial tension test.

$$P_{sl} + P_{br} = P_{s(LOAD)} \tag{18}$$

In the case of conventional concrete, since the fiber bridging effect at cracks does not exist and P_{br} is equal to zero, tensile force of rebar at loaded end, $P_{s(LOAD)}$, is the same as that at crack position, P_{sl}. On the other hand, in the case of FRCC, tensile force of rebar at crack, P_{sl}, is smaller than that at loaded end, $P_{s(LOAD)}$, because of the bridging effect of fibers, P_{br}. The relationship between the forces at crack and at loaded end is expressed as Eq.(19) by using stain of rebar at crack position, ε_{sl}, at loaded end, $\varepsilon_{s(LOAD)}$, and fiber bridging stress, σ_{br}.

$$\varepsilon_{sl} + \frac{1}{npE_c}\sigma_{br} = \varepsilon_{s(LOAD)} \tag{19}$$

While the steel strain obtained from uniaxial tension test is corresponding to $\varepsilon_{s(LOAD)}$, the steel strain given by Eq.(17) is corresponding to ε_{sl}. Therefore, the test results cannot be directly compared with the theoretical results obtained from Eq.(17). However, it is difficult to measure the steel strain at crack position in uniaxial tension test. To solve this problem, theoretical formula which is expressed by $\varepsilon_{s(LOAD)}$ instead of ε_{sl} is also derived as Eq.(20) by substituting Eq.(17) to Eq.(19).

$$\varepsilon_{s(LOAD)} = \frac{k_{bo}\varphi_s}{8A_c\{\sigma_{cr} - \sigma_{br}(w_{cr})\}}{w_{cr}}^2 + \frac{1+np}{2npE_c}\{\sigma_{cr} + \sigma_{br}(w_{cr})\} \tag{20}$$

Eq.(20) gives the relationship between strain of rebar at loaded end and crack width when a new crack generates. In the next chapter, theoretical results given by Eq.(20) is compared with the test results obtained in Chapter 3 and the adaptability of this theoretical solution is confirmed.

Chapter 3 Uniaxial Tension Test

3.1 Introduction

In this chapter, uniaxial tension test is conducted for steel-reinforced FRCC prism specimens using aramid and PVA fibers to measure the crack width experimentally. The crack opening behavior is compared each other through the steel strain – crack width relationships obtained from the loading test.

3.2 Experiment Outline

3.2.1 Specimens

Figure 3.1 shows the dimensions of specimens and **Table 3.1** shows the list of specimens. The specimen is FRCC prism with square cross section and its total length is 600mm. One steel deformed rebar D16 (SD490: specific yield strength of 490MPa) was arranged in the center of cross section along the axial direction. The experimental parameters are cross-sectional size of prism, fiber types and fiber volume fraction. The cross section was set to 100mm, 120mm, and 140mm square for A, B, and C series of specimens, respectively. To control the cracking position, slits were set on both sides of specimen at 100mm spacing. The depth of silt was changed in accordance with the cross-sectional size as the cross-sectional area at the slit position was reduced to 60% area of full section. In order not to disturb the fiber orientation, the slits were installed after demolding using a concrete cutter. Aramid and PVA fibers were used for FRCC. Fiber volume fraction were set to 0% (mortar), 1%, and 2% for each fiber. Three specimens were tested for each combination of test parameters.

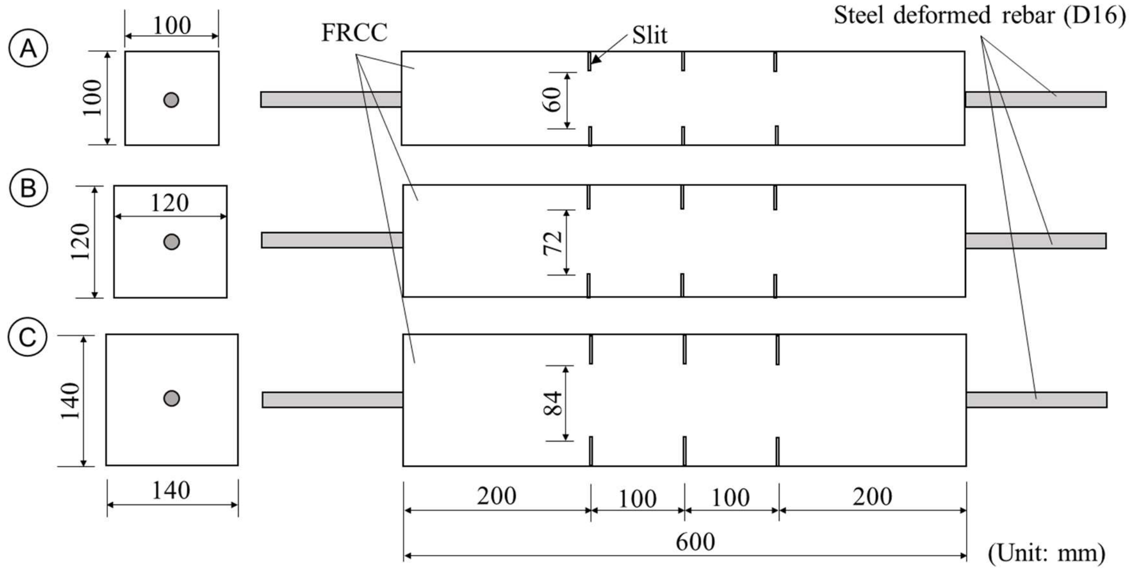

Figure 3.1 Dimension of specimens

Table 3.1 List of specimens

Type	ID	Fiber		Cross-sectional size (Sectional size at slit)	Common factor
		Types	Volume fraction		
No Fiber-A	1~3	—	—	100mm×100mm (100mm×60mm)	Length: 600mm Number of slits: 6 Spacing of slits: 100mm Steel rebar: D16 (SD490)
AF1-A	1~3	Aramid	1.0%		
AF2-A	1~3		2.0%		
PVA1-A	1~3	PVA	1.0%		
PVA2-A	1~3		2.0%		
No Fiber-B	1~3	—	—	120mm×120mm (120mm×72mm)	
AF1-B	1~3	Aramid	1.0%		
AF2-B	1~3		2.0%		
PVA1-B	1~3	PVA	1.0%		
PVA2-B	1~3		2.0%		
No Fiber-C	1~3	—	—	140mm×140mm (140mm×84mm)	
AF1-C	1~3	Aramid	1.0%		
AF2-C	1~3		2.0%		
PVA1-C	1~3	PVA	1.0%		
PVA2-C	1~3		2.0%		

3.2.2 Used Materials

Table 3.2 shows the dimensions and mechanical properties of both aramid and PVA fiber used in FRCC and **Figure 3.2** shows the visual appearance of the fibers. Aramid fiber is the same one used in the previous study [13], and PVA fiber is also the same one used in the previous studies [12,14].

Table 3.3 shows the mixture proportion and mechanical properties of FRCC. The mixture proportion is also same one designed in the previous studies [12, 13]. Since the fresh FRCC shows self-compacting characteristics, FRCC was filled into the mold by pouring from one end of the mold as shown in **Figure 3.3** paying attention not to disturb the fiber orientation. The compressive strength and elastic modulus of FRCC shown in **Table 3.3** were obtained from compression test of ϕ100mm x 200mm cylinder test pieces.

Table 3.4 shows the mechanical properties of reinforcing bar. Steel deformed reinforcing bar with nominal diameter of 16mm and specific yield strength of 490MPa was utilized.

Table 3.2 Dimensions and mechanical properties of fibers

Fiber	Length (mm)	Diameter (mm)	Tensile strength (MPa)	Elastic modulus (GPa)
Aramid	30	0.50	3432*	73*
PVA	12	0.10	1200	28

* Properties obtained by original yarns

(a) (b)

Figure 3.2 Visual appearance of fibers: (a) Aramid; (b) PVA

Table 3.3 Mixture proportion and mechanical properties of FRCC

Type	Unit weight (kg/m^3)					Compressive strength (MPa)	Elastic modulus (GPa)
	Water	Cement	Sand	Fly ash	Fiber		
No Fiber	380	678	484	291	0	52.5	18.1
AF1					13.9	48.2	18.1
AF2					27.8	47.5	16.4
PVA1					13	49.5	17.6
PVA2					26	41.2	15.6

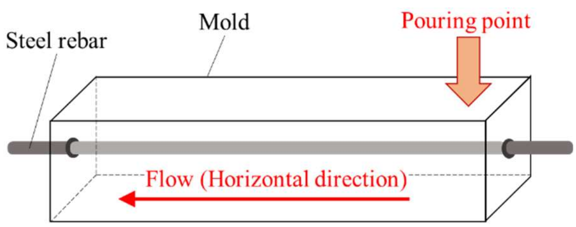

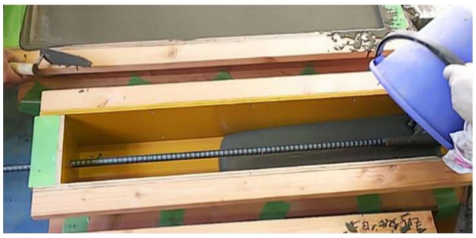

Figure 3.3 Casting method of FRCC

Table 3.4 Mechanical properties of reinforcing bar

Type	Yield strength (MPa)	Elastic modulus (GPa)	Yield strain (μ)	Tensile strength (MPa)
D16 (SD490)	516	198	2604	709

3.2.3 Loading and Measurement

Figure 3.4 shows the set-up of loading and measurement. Uniaxial monotonic tension loading is conducted under the controlled displacement using universal testing machine. The total deformation was measured by two linear variable displacement transducers (LVDTs) to confirm the yielding of steel rebar. Crack width at each slit position was measured by Pi-type LVDTs arranged at 100mm spacing on both side of the specimens. The criteria of defining crack width is explained in detail in section 3.3.1. Visible crack observations were recorded in each loading measurement step.

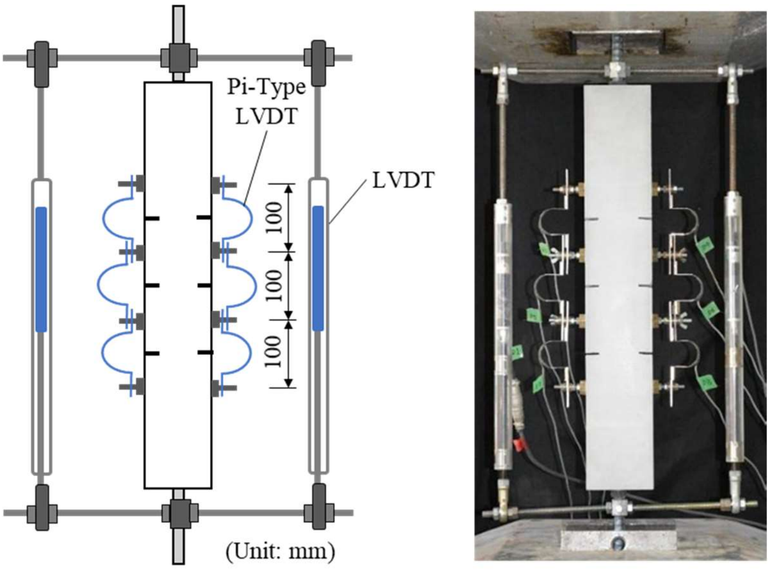

Figure 3.4 Set-up of loading and measurement

3.3 Experiment Results

3.3.1 Crack Patterns and Crack Width

Figure 3.5 shows the examples of crack patterns after yielding of steel rebar. The specimens with fewer cracks in longitudinal direction are selected as the examples in each parameter. Cracks took place at slit positions before steel rebar yielding in all specimens. However, branched cracks at slit positions or another crack at no-slit position were observed in many specimens. The total number of cracks increased with decreasing of cross-sectional area and increasing of fiber volume fraction.

In the case of a single crack at slit position, the crack width is obtained by averaging two values measured by Pi-type LVDTs on both sides of specimen ignoring the elastic deformation of FRCC. After the second crack was observed in one measurement region as shown in **Figure 3.6**, the measured data at that region was excluded from the evaluation, so that the measured crack width corresponds to a single crack.

	No Fiber	AF1	AF2	PVA1	PVA2
A series (100mm×100mm)	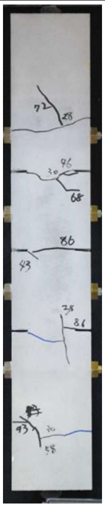	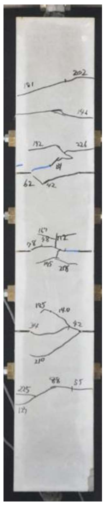	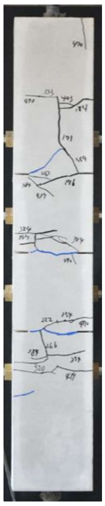	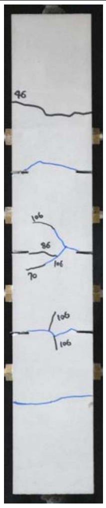	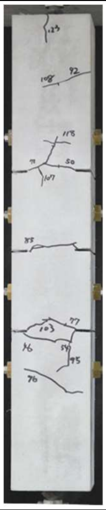
B series (120mm×120mm)	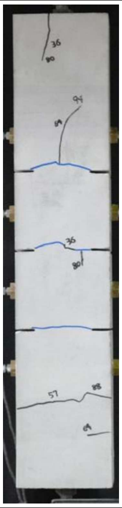	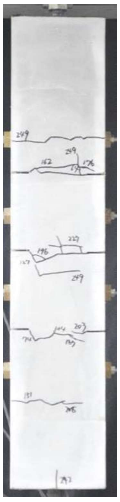	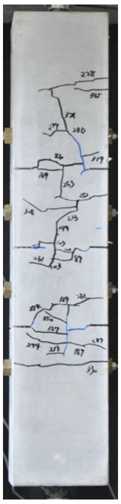	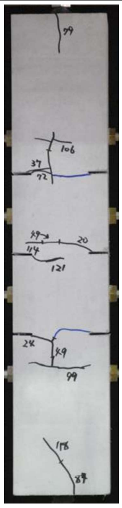	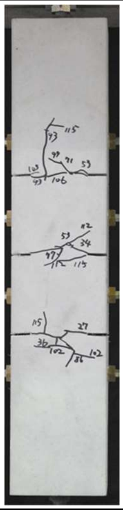
C series (140mm×140mm)	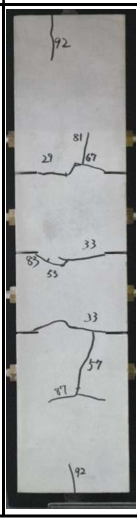	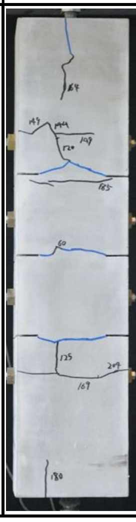	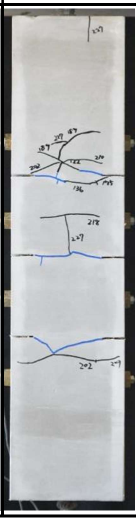	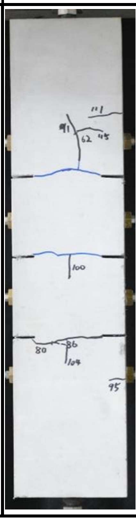	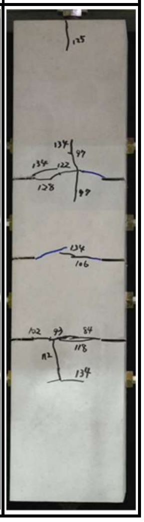

Figure 3.5 Examples of crack patterns (after yielding of steel rebar)

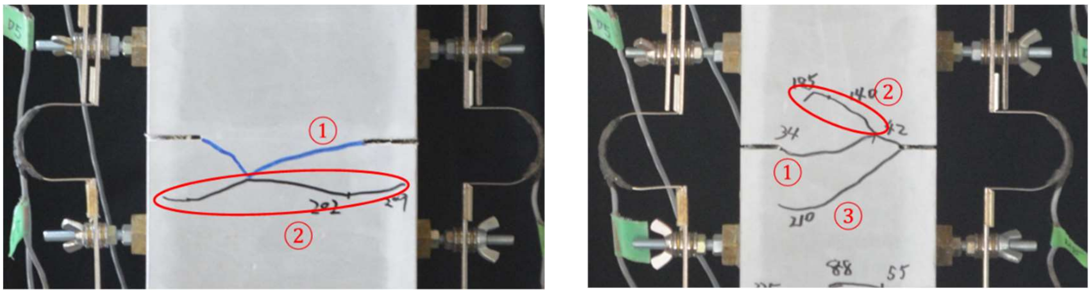

(①: first crack, ②: second crack, ③: third crack)

Figure 3.6 Examples of cracking process

3.3.2 Steel Strain – Crack Width Relationship

Figure 3.7 shows the steel strain – crack width relationships obtained from the loading test. The steel strain is calculated from the measured tensile load by using the elastic modulus of reinforcing bar previously shown in **Table 3.4**. The crack width of these curves increases just after the beginning of the loading due to the deformation of FRCC in the measurement region. To compare the crack opening behavior, the average line of test results is also shown in **Figure 3.7** as dotted line. Each experimental curve is approximated with proportional relations ($y = a \cdot x$) by using the least square method and the average lines are determined by averaging these coefficients, a, in each parameter.

The slope of average lines decreases with increasing of cross-sectional size by comparing among No Fiber-A, B and C specimens. Since the number of cracks decreases with increasing of cross-sectional area, crack opening tends to be larger at the same steel strain. In the case of FRCC specimens, the influence of sectional size is less than the case of No Fiber specimens because of the fiber bridging effect.

By comparing the average lines in the same series of cross section, increasing of fiber volume fraction increases the slope of the average lines both in AF and PVA specimens. Crack opening tends to be smaller with increasing of fiber volume fraction because the fiber bridging force at crack increases. On the other hand, by comparing the average lines between AF and PVA specimens in the same fiber volume fraction and the same series of cross section, the difference of the slope is unclear. It can be said that it is difficult to compare the crack opening behavior only by the average lines, hence, the difference is discussed in Chapter 4 by using the theoretical curves.

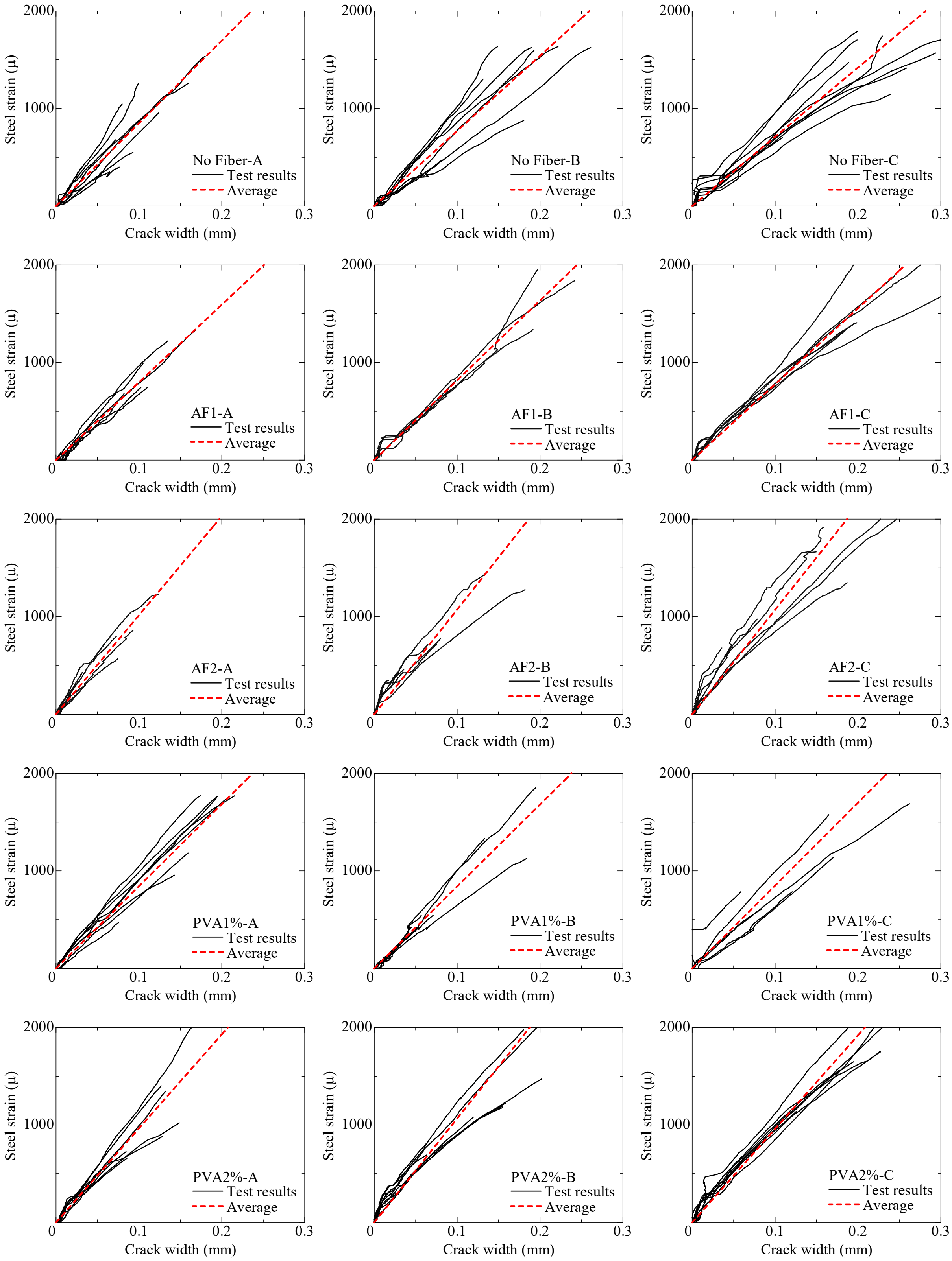

Figure 3.7 Steel strain – crack width relationships

Chapter 4 Adaptability of Theoretical Solution of Crack Width Prediction

4.1 Introduction

In this chapter, theoretical curves of steel strain - crack width relationships are calculated using the proposed formula described in Chapter 2 and compared with the test results obtained in Chapter 3 to confirm the adaptability of the solution. In addition, parametric study of theoretical curves is conducted using the models of bridging law for 4 types of fibers, and the crack width is compared each other to understand the influence of fiber types on crack width evaluation.

4.2 Bridging Law Model

4.2.1 Aramid and PVA-FRCC

At first, the bridging law of aramid-FRCC (V_f = 2%) is expressed by bilinear model as similar with the model for PVA-FRCC [14] in which the characteristic points of the model are given by the function of fiber orientation intensity. The details can be found in Appendix. The maximum point (δ_{max}, w_{max}) and the point when the bridging stress becomes zero (w_{tu}, 0) are expressed by the function of fiber orientation intensity, k, as follows.

$$\sigma_{max} = 2.0k^{0.30} \text{ (MPa)} \tag{21}$$

$$w_{max} = 0.60k^{0.07} \text{ (mm)} \tag{22}$$

$$w_{fu} = 9.3k^{0.05} \text{(mm)} \tag{23}$$

In the case of PVA-FRCC, the bridging law of fiber volume fraction 2% is expressed by tri-linear model in the previous study [14]. The maximum point (δ_{max}, σ_{max}), the second folding point (δ_2, σ_2) and the point when the bridging stress becomes zero (δ_{tu}, 0) are also given by the function of k as follows.

$$\delta_{max} = 0.20k^{0.18} \text{ (mm)} \tag{24}$$

$$\sigma_{max} = 2.0k^{0.30} \text{ (MPa)} \tag{25}$$

$$\delta_2 = 0.45 \text{ (mm)} \tag{26}$$

$$\sigma_2 = 0.60k^{0.73} \text{ (MPa)} \tag{27}$$

$$\delta_{fu} = 6 \text{ (mm)} \tag{28}$$

The value of k is decided based on the results of previous study in which the size effect on fiber orientation of FRCC has been investigated [23].

In that study, four-point bending test was conducted for three different dimensions of PVA-FRCC prism specimens with 40 mm x 40 mm, 100 mm x 100 mm, and 180 mm x 280 mm in cross-section. The section analysis was performed by using bridging law of PVA fiber considering several cases of fiber orientation intensity, k. The test results of 100 mm x 100 mm cross section specimens showed the best agreement with the analytical results in bending strength by assuming k = 1.

For these reasons, k = 1 is also adapted for Eq.(21) – Eq.(28), and the models shown in **Figure 4.1** are used for the calculation of theoretical curves. The models of V_f = 1% and 0.5% in both fiber types are assumed that bridging force is half and quarter as much as that of V_f = 2%, respectively. The models of V_f = 0.5% is used only in the parametric study. When the bridging law is substituted for the theoretical formula, bridging stress is multiplied by 0.6 times, which corresponds to the ratio of cross-sectional area at slit position to the whole section, in order to take the absence of bridging fibers at slit into account. In No Fiber specimens, bridging stress is substituted by zero in the formula.

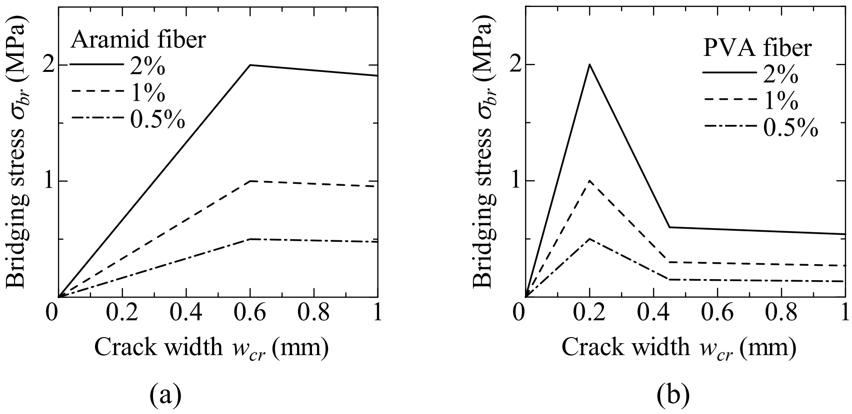

Figure 4.1 Adapted bridging law models in theoretical formula
(a) Aramid-FRCC; (b) PVA-FRCC

4.2.2 PP and Steel-FRCC

In addition to aramid and PVA-FRCC, the theoretical curves are calculated using the bridging law models of PP and steel-FRCC for the parametric study. **Table 4.1** shows the dimensions and mechanical properties of both PP and steel fiber and **Figure 4.2** shows the visual appearance of the fibers. These fibers are the same one used in the previous studies [24,25].

The bridging law (bridging stress – crack width relationship) of PP and steel-FRCC are calculated similarly as the previous study [13]. The individual fiber pullout models obtained in the previous studies (PP [24], steel [25]) are adapted for the pullout load of an individual fiber. **Table 4.2** shows the used parameters for pullout behavior of an individual fiber for the calculation of bridging law. The snubbing effect and the reduction of apparent rupture strength are also considered, and the values listed in the table are adapted for calculation. The fiber orientation is assumed to be the same as the case of calculating the bridging laws for aramid and PVA-FRCC in the previous section, and the value k = 1 is adapted for the fiber orientation intensity.

Table 4.1 Dimensions and mechanical properties of fibers

Fiber	Length (mm)	Diameter (mm)	Tensile strength (MPa)	Elastic modulus (GPa)
PP	30	0.70	580	4.9
Steel	13	0.16	2825	210

(a) (b)

Figure 4.2 Visual appearance of fibers: (a) PP; (b) Steel

Table 4.2 Parameter for individual fiber pullout behavior

Parameter		Input	
		PP [24]	Steel [25]
Pullout model (ψ = 0)	Maximum pullout load, $P_{max,0}$ (N)	$25\times l_b^{0.61}$	$1.3\times l_b$
	Crack width at $P_{max,0}$, $\delta_{max,0}$ (mm)	$0.062\times l_b$	$0.03\times l_b$
Snubbing effect by ψ	Maximum pullout load, $P_{max,\psi}$(N)	$P_{max,0}\times e^{0.21\psi}$	$P_{max,0}\times e^{(2.6-0.3l_b)\psi}$
	Crack width at $P_{max,\psi}$, $\delta_{max,\psi}$(mm)	$\delta_{max,0}\times e^{1.4\psi}$	$\delta_{max,0}$
Apparent rupture strength, σ_{fu} (MPa)		$491\times e^{-0.36\psi}$	2825

Notation: ψ = fiber inclination angle to x-axis (rad.)
l_b = embedded length of fiber (mm)

Figure 4.3 shows the calculation results of bridging law for PP and steel-FRCC. Fiber volume fraction is set to 2%. The obtained bridging law is modeled subjecting to the region of crack width smaller than 1 mm as shown in **Figure 4.4**. The bridging law of PP-FRCC is modeled as elastic model connecting the origin and the point at crack width = 1 mm, and that of steel-FRCC is modeled as bilinear model connecting the origin, the point at maximum bridging stress and that at crack width = 1 mm.

Figure 4.5 shows the used bridging law models of PP and steel-FRCC in the calculation of theoretical curves for the parametric study. The models of V_f = 1% and 0.5% in both fiber types are assumed that bridging force is half and quarter as much as that of V_f = 2%, respectively.

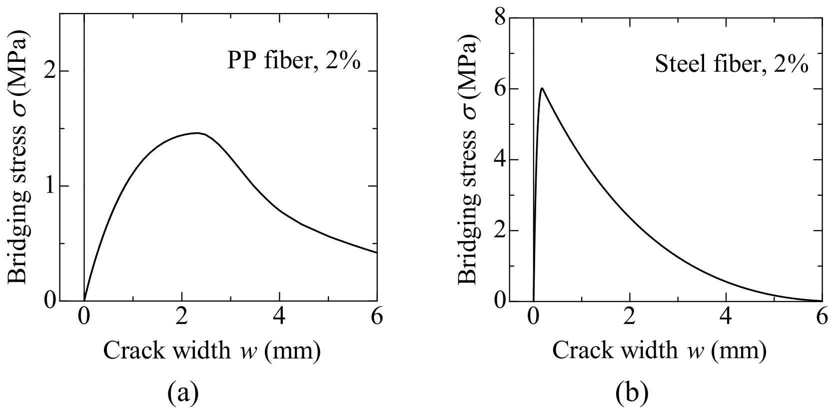

Figure 4.3 Calculation result of bridging law: (a) PP-FRCC; (b) Steel-FRCC

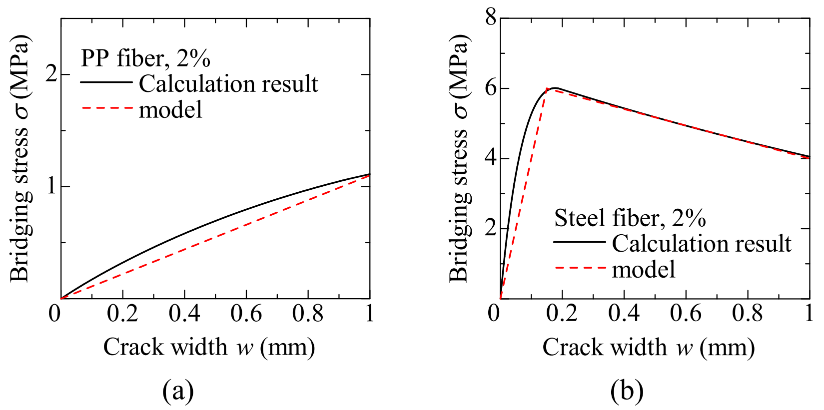

Figure 4.4 Modeling of bridging law: (a) PP-FRCC; (b) Steel-FRCC

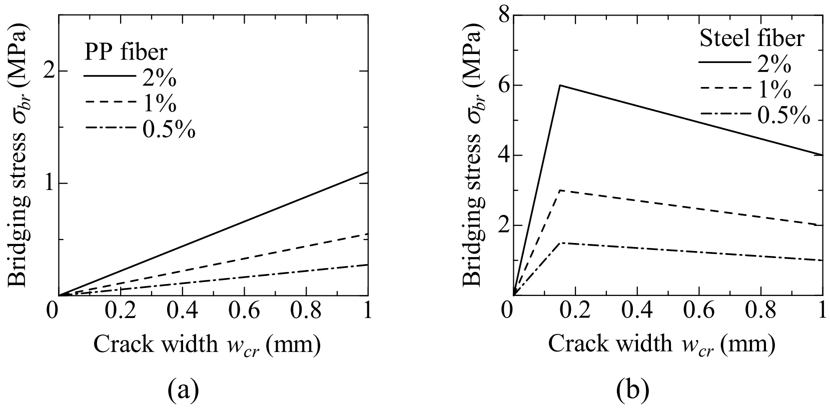

Figure 4.5 Adapted bridging law models in theoretical formula
(a) PP-FRCC; (b) Steel-FRCC

4.3 Other Constitutive Laws

Table 4.3 shows the used parameters in theoretical formula, Eq.(20). The nominal values are used in cross-sectional area and perimeter of steel rebar. Sectional size of FRCC agrees with the dimensions of specimens described in Chapter 3. The elastic modulus of steel rebar and FRCC is obtained from the material tests explained in Chapter 3.

Cracking strength of FRCC is calculated from the test results of uniaxial tension test because it is difficult to obtain the value directly from the material test. According to the steel strain – crack width relationships of No Fiber-C, AF1-B, AF2-B, PVA1-C and PVA2-C specimens shown in **Figure 3.7**, rapid increasing of crack width is observed in the small range of steel strains. It is considered that the cracks start opening at those steel strains. The values are 324μ, 239μ, 318μ, 420μ and 492μ in No Fiber, AF1, AF2, PVA1 and PVA2 specimens, respectively. These values are converted to the tensile load by using elastic modulus and cross-sectional area of steel rebar. The tensile loads are divided by the cross-sectional area of FRCC at slit position (B series: 120 mm x 72 mm, C series: 140 mm x 84 mm) and cracking strength is calculated as shown in **Table 4.3**.

Table 4.3 Used parameters in theoretical formula

				No Fiber	AF1	AF2	PVA1	PVA2
Steel rebar	Cross-sectional area	A_s	mm^2	198.6				
	Perimeter	φ_s	mm	50				
	Elastic modulus	E_s	GPa	198				
FRCC	Cross-sectional area	A_c	mm^2	A:100^2, B:120^2, C:140^2				
	Elastic modulus	E_c	GPa	18.1	18.1	16.4	17.6	15.6
	Cracking strength	σ_{cr}	MPa	1.03	1.09	1.45	1.33	1.56

Bond stress – slip relationship is assumed from the test result of steel rebar pullout test using PVA-ECC [26] which compressive strength is almost the same as FRCC used in this study. Based on the test result of PVA-ECC specimens with D16 rebar and cover thickness of 32mm, bond stiffness is assumed as k_{bo} = 50N/mm^3 and bond stress – slip relationship is modeled as shown in **Figure 4.6**.

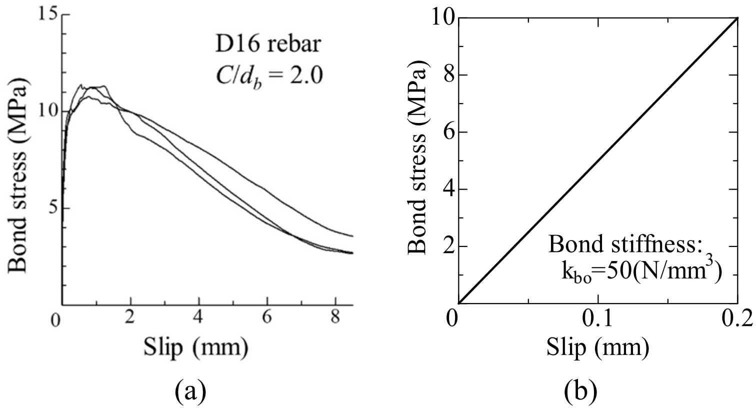

Figure 4.6 Bond stress - slip relationship
(a) Examples of test results; (b) Model

4.4 Adaptability of Crack Width Prediction

Figure 4.7 shows the steel strain – crack width relationships obtained from both uniaxial tension tests and theoretical formula, Eq.(20). While the test results show the crack opening behavior of each crack, theoretical curve shows the possible maximum crack width as previously mentioned in Chapter 4. The theoretical curves of PVA1-B and C specimens show folding points of the slope at crack width = 0.2 mm. This is because the fiber bridging law model of PVA-FRCC has the folding point at crack width = 0.2 mm as shown in **Figure 4.1**.

The curves of measured crack widths in most of the specimens locate in the area of crack width smaller than the theoretical curves. It can be said that the theoretical formula shows a good adaptability with the experimental results. However, the crack width of some test results exceeds the theoretical curve especially in C series specimens. In this study, fiber orientation intensity is assumed to be $k = 1$ regardless of sectional size of the specimen. It has been reported that the increasing of sectional size decreases fiber orientation intensity and fiber bridging stress of bridging law [23]. It is considered that bridging effect is overestimated, and crack width is underestimated in theoretical formula especially in the specimens with larger cross section.

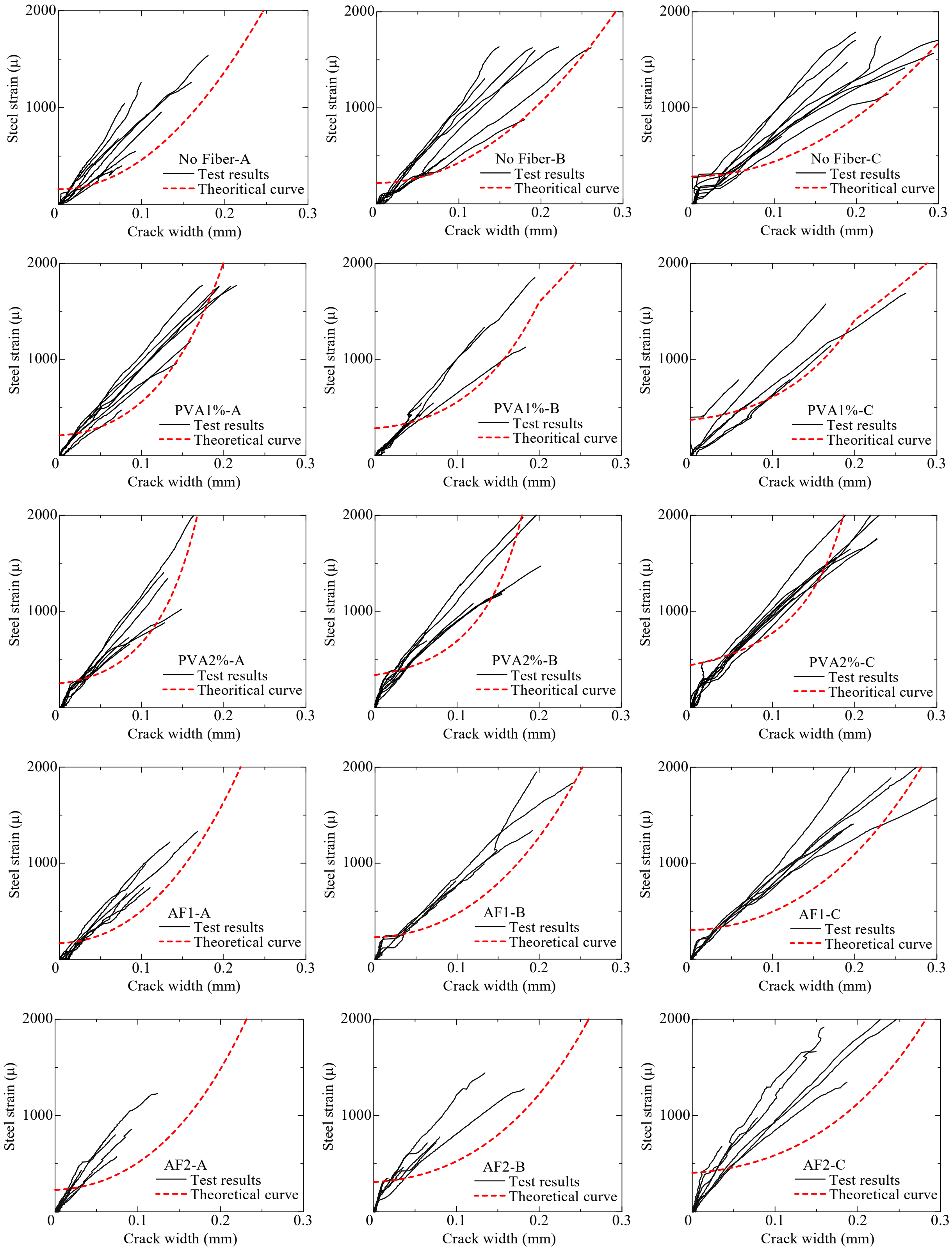

Figure 4.7 Comparison between theoretical curve and test results

Figure 4.8 shows the comparison of theoretical curves, which expresses the possible maximum value of crack width. By comparing the curves among No Fiber, PVA1 and PVA2 specimens in the same series of cross section, the crack width at the same steel strain is smaller in specimens with larger volume fraction of fibers. This is because the fiber bridging force increases with increasing of fiber volume fraction.

In the case of aramid fiber, although the crack width in AF1 specimen is smaller than that in No Fiber specimen, there are few differences of crack width between AF1 and AF2 specimens. This is because the theoretical curve is influenced not only by the bridging law but also by the cracking strength of FRCC. While the bridging force increases with increasing of fiber volume fraction, the cracking strength also increases, hence, the difference of crack width between AF1 and AF2 specimens becomes small.

By comparing the curves between AF and PVA specimens, the crack width is smaller in PVA1 specimen than AF1 and AF2 specimens. This is because the initial slope of bridging law of PVA fiber is larger than that of aramid fiber. According to the previous study [27], it is considered that the alcohol group in a PVA molecule brings good bond in matrix, hence, PVA fiber shows good bridging performance especially in the small range of crack width. However, the crack width rapidly increases after 0.2 mm in PVA1-B and C specimens because the crack width reaches to the softening branch of bridging law resulting from the rupture of fibers [12]. On the other hand, rapid crack opening is not observed in the curves of AF specimens because aramid fiber shows higher tensile strength than PVA fiber.

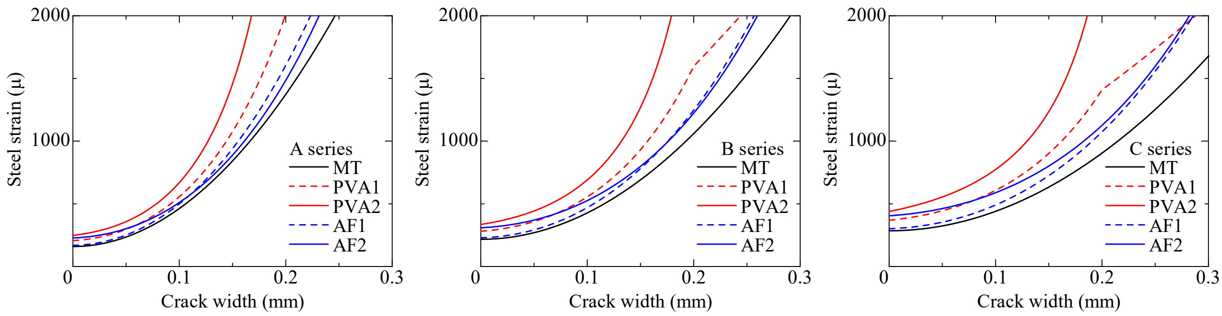

Figure 4.8 Comparison of theoretical curves

4.5 Influence of Fiber Types on Crack Width Evaluation

The parametric study of theoretical curves given by Eq.(20) is conducted using the models of bridging law for 4 types of fibers, and the crack width is compared each other. **Figure 4.9** shows the dimension of steel-reinforced FRCC prism for the calculation of theoretical curves. The prisms correspond to A and C series specimens for uniaxial tension test in Chapter 3 except for the absence of slits. The length of prism is arbitrary because the length is not required to calculate theoretical curves. The theoretical curves are calculated by varying the models of bridging law. The bridging law models of aramid, PVA, PP and steel-FRCC shown in **Figure 4.1** and **Figure 4.5** are adapted for the theoretical formula, Eq.(20). The other parameters are set to be constant regardless of the types of fibers to compare the influence of bridging law on crack width clearly, and the values of PVA 2% (PVA2) listed in **Table 4.3** and bond stiffness of $k = 50$ N/mm^3 shown in **Figure 4.6** are used in every cases.

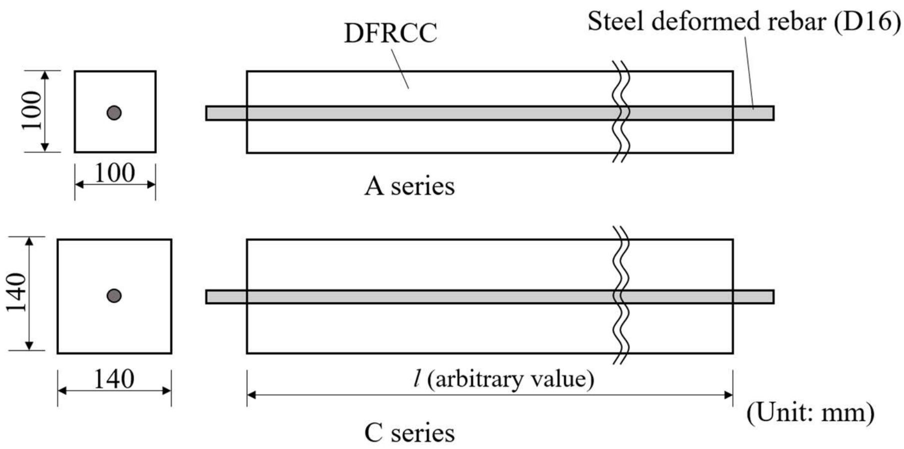

Figure 4.9 Dimension of steel-reinforced FRCC prism

Figure 4.10 shows the comparison among theoretical curves obtained by the parametric study. The theoretical curves of No Fiber specimens are also shown in each graph to compare the fiber bridging effect. According to the figures, increasing of fiber volume fraction decreases the crack width at the same steel strain. This tendency can be observed in every types of fibers. By comparing among the curves with different fiber types in the same series of cross section and fiber volume fraction, the crack width becomes smaller in the order of PP, aramid, PVA and steel-FRCC. This is because the initial slopes of the bridging law models become larger in the same order.

Especially in the case of steel-FRCC, the crack width is much smaller even in specimen with fiber volume fraction 0.5% than the other types of specimen. This is because the initial slope and the maximum bridging stress of the bridging law model for steel-FRCC are larger than the other bridging law models. It is considered that this is brought by the following characteristics of steel fiber:

- Steel fiber has high tensile strength and does not rupture at the pullout process from matrix.
- The elastic modulus of steel fiber is large
- The snubbing effect resulting from the fiber inclination angle is large in steel-FRCC

On the other hand, in the case of PP-FRCC, the difference of crack width is small by comparing between the curves of PP-2% and No Fiber. This is because the initial slope of the bridging law model for PP-FRCC is small, which is brought by the following characteristics of PP fiber:

- The elastic modulus of PP fiber is small
- The bond stiffness between PP fiber and cementitious matrix is small.

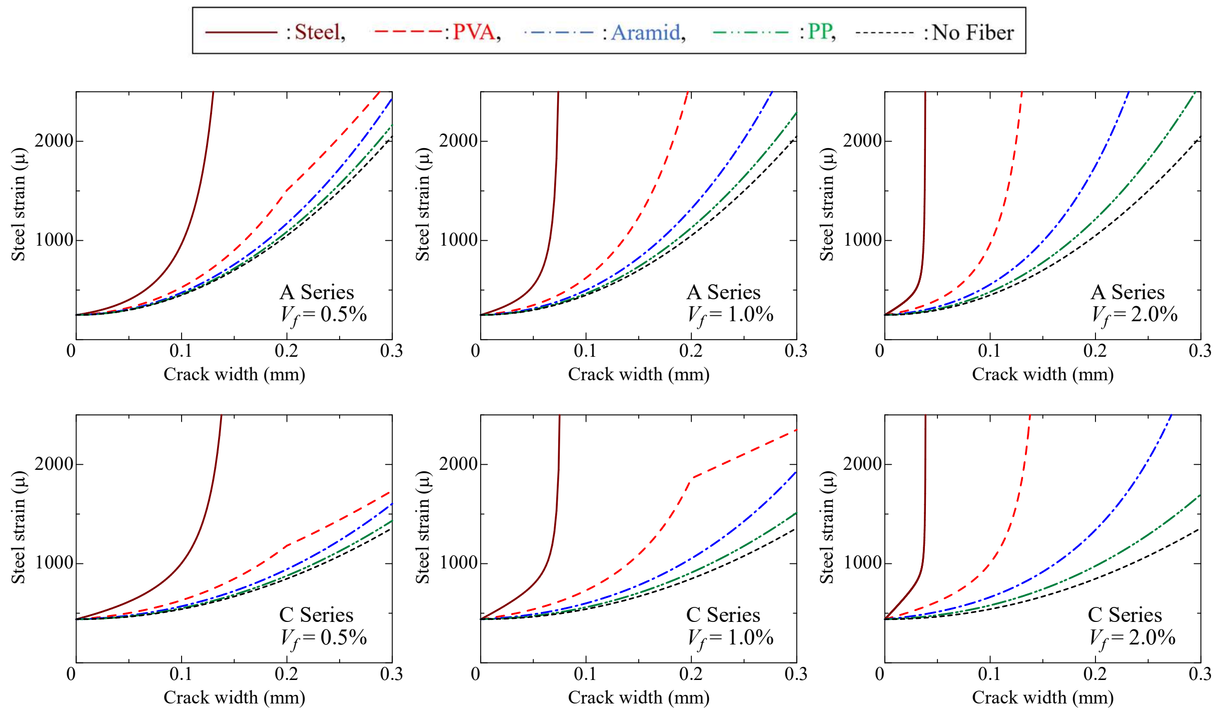

Figure 4.10 Comparison of theoretical curves

Chapter 5 Conclusion

In this study, a simplified method to predict crack width in steel-reinforced FRCC prism was derived by theoretical calculation considering both fiber bridging effect and bond interaction between FRCC and reinforcing bar. The uniaxial tension test was conducted for 45 specimens varying the sectional size of prism, fiber types and fiber volume fraction to measure the crack width experimentally, and the proposed method was adapted for the evaluation of the test results. The main conclusions of this research are summarized as below.

(1) The steel strain – crack width relationship was given by a simple formula using bond constitutive law and fiber bridging law in addition to the material parameters of FRCC and rebar.

(2) Theoretical curves were calculated by using the proposed formula and compared with the test results. The theoretical curves showed a good adaptability to evaluate the crack width in each test parameter.

(3) According to the evaluation results using theoretical curves, crack width was smaller in PVA-FRCC by comparing with aramid-FRCC because the initial slope of bridging law is larger. However, crack width rapidly increased when the crack width reaches to the softening branch of the bridging law in PVA-FRCC, while this tendency was not observed in aramid-FRCC because of the high tensile strength of aramid fiber.

(4) Parametric study of theoretical curves was conducted using the models of bridging laws for 4 types of fibers. The crack width at the same steel strain becomes smaller in the order of PP, aramid, PVA and Steel fiber because the initial slope of the bridging laws become larger in the same order.

Acknowledgements

I would like to express my deepest gratitude to my academic supervisor, Professor Toshiyuki Kanakubo, for his precious guidance, constructive supervision, priceless feedback, and pleasant communication during this research project. Without his encouragement and support, I could not finish my research and complete this thesis. His extensive research experience and keen insight have impressed me deeply and will certainly encourage me for the rest of my life as a researcher.

I would like to thank my vice-academic supervisor Associate Professor Akira Yasojima and a technical staff member Mr. Kojima, for their extremely important assistance on my experiment and their valuable comments on my research.

I would also like to thank all the members in this laboratory for their kind support and creating such a nice working environment. Special thanks go to Keisuke Namiki and Takumi Koba for their help in executing experimental work.

At last, special thanks are also expressed to my dearest parents for their support and understanding.

Appendix

Modeling of Bridging law for Bundled Aramid-FRCC

The modeling method of aramid-FRCC referred in Chapter 4 is described in this Appendix. Aramid fiber is a bundled fiber with nominal diameter of 500 μm. The visual appearance of the used fiber is shown in **Figure A.1**. The original yarns of aramid fibers with nominal diameter of 12 μm are twisted to form a thick individual fiber, and sized not to unravel in matrix. The tensile strength and elastic modulus of the original yarn is 3432 MPa and 73 GPa, respectively. Chopped fibers with length of 30 mm are utilized for mixing FRCC.

(a)

(b)

Figure A.1 Visual appearance of used aramid fiber:
(a) Chopped aramid fibers for mixing FRCC; (b) Condition of bundling of yarns

The bridging law, i.e., bridging stress - crack width relationship is calculated as similar with the previous study [12]. In a FRCC prism subjected to the uniaxial tension, fibers bridge through crack plane as shown in **Figure A.2** (a). Fibers are distributed in crack plane with various inclination angle. The pullout behavior and rupture strength of the individual fiber is affected by the fiber inclination angle that is defined as shown in **Figure A.2** (b). The angle, ψ, expresses the fiber inclination angle to x-axis, and angles, θ and ϕ, express ones between x-axis and projected lines of the fiber to x-y plane and z-x plane, respectively. The bridging stress can be calculated by summation of forces carried by individual fibers bridging through crack plane considering the probability density function (PDF) for fiber inclination angles and fiber centroidal location as given by Eq.(A.1).

$$\sigma_{bridge} = \frac{P_{bridge}}{A_m} = \frac{V_f}{A_f} \cdot \sum_h \sum_j \sum_i P_{ij}(w, \psi) \cdot p_{xy}(\theta_i) \cdot p_{zx}\left(\phi_j\right) \cdot p_x(y_h, z_h) \cdot \Delta\theta \cdot \Delta\phi \cdot (\Delta y \cdot \Delta z) \quad (\mathrm{A.1})$$

where,

σ_{bridge} = bridging stress,

P_{bridge} = bridging force (= total of pullout load),

A_m = cross-sectional area of matrix,

V_f = fiber volume fraction,

A_f = cross-sectional area of an individual fiber,

w = crack width,

$P(w,\psi)$ = pullout load of an individual fiber,

p_{xy}, p_{zx} = PDF (elliptic distribution) for fiber inclination angle,

p_x = PDF for fiber centroidal location (assumed to be constant),

$\Delta y \cdot \Delta z$ = area of infinitesimal element on crack plane.

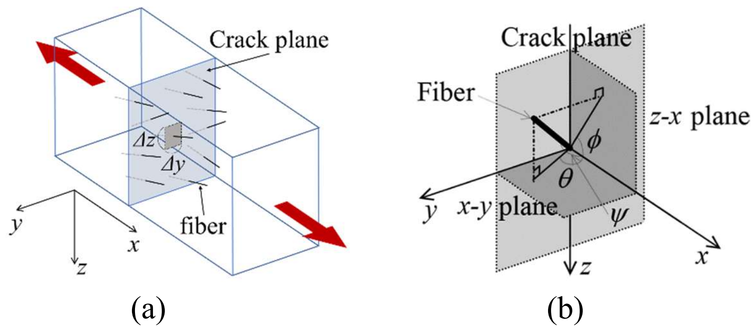

Figure A.2 Schematic drawing for the calculation of bridging law
(a) Fibers bridging through crack plane; (b) Definition of fiber inclination angle

The bilinear model proposed in the previous study [13] is adapted for the pullout load of an individual fiber, $P(w,\psi)$. The elliptic distribution [12] is adopted for the PDF, p_{xy} and p_{zx}, for fiber inclination angles. The elliptic distribution is defined by two parameters; principal orientation angle, θ_r (argument of one radius of elliptic function) and orientation intensity, k (ratio of the two radii of elliptic function). The fiber orientation can be expressed by these parameters. The random orientation is given by k = 1. Fibers tend to orient toward θ_r when the value of k is larger than 1, while fibers tend to orient toward the perpendicular to θ_r when the value of k is smaller than 1.

The PDF for fiber centroidal location, p_x, is set to constant assuming the uniform distribution of fibers along x-axis. The parameters for the calculation are summarized in **Table A.1**. Fiber volume fraction and principal orientation angle is set to 2% and 0 degree, respectively.

Table A.1 Parameters for calculation of bridging law

Parameter		Input
Fiber volume fraction, V_f (%)		2.0
Length of fiber, l_f (mm)		30
Diameter of fiber, d_f (mm)		0.5
Apparent rupture strength of fiber, σ_{fu} (MPa) [13]		$\sigma_{fu} = 1080 \cdot e^{-0.667\psi}$
Bilinear model [13]	Maximum pullout load, P_{max} (N)	$P_{max} = 7.47 \cdot l_b$
	Crack width at P_{max}, w_{max} (mm)	$w_{max} = 0.13 \cdot l_b^{0.64}$

Notation: ψ = fiber inclination angle to x-axis (rad.)
l_b = embedded length of fiber (mm)

The calculated bridging laws for the orientation intensity k from 0.1 to 10 are shown in **Figure A.3**. The left figure shows whole curves, and the right figure focuses on small ranges until w = 5 mm. The bridging laws shown in the figures are calculated with 0.1 intervals of k in the case of $k < 1$, and with 1 interval when $k > 1$. The bridging stress in **Figure A.3** do not include the tensile stress carried by the matrix before cracking to exhibit the tensile stress due to only bridging force of fibers. Each curve shows maximum bridging stress at about w = 0.6 mm. After that, bridging stress decreases moderately with increasing of crack width. This is because the most of fibers do not rapture and they gradually pulled out from the matrix. Bridging stress becomes zero when the value of crack width reaches to 15 mm (half length of the fiber) because all fibers are completely pulled out from matrix. On the other hand, by comparing each curve, the maximum bridging stress remarkably increases with increasing of the value of k. In other word, bridging stress becomes larger when the fibers strongly oriented to the normal direction of crack surface.

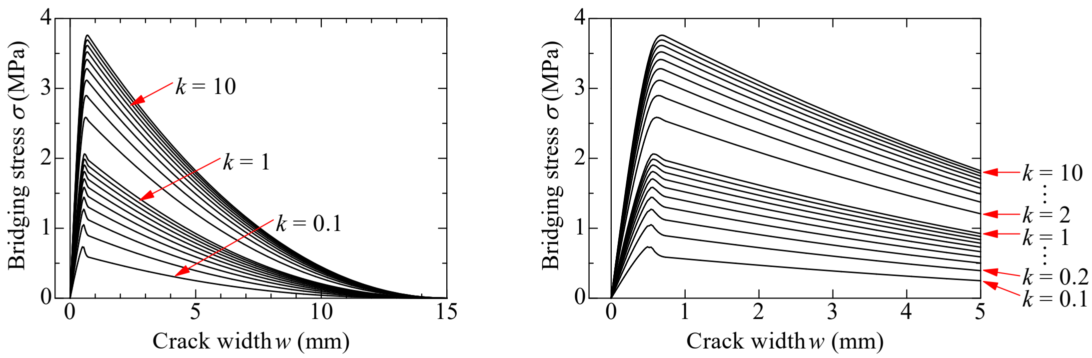

(a) (b)

Figure A.3 Calculation results of bridging law: (a) w = 0~15 mm; (b) w = 0~5 mm

The calculated bridging laws are modeled by simple forms considering fiber orientation. From **Figure A.3**, the bridging law is simply characterized by two regions, i.e., curve until the maximum stress and softening branch. Therefore, the bridging law is modeled by bilinear model as shown in **Figure A.4**. The model has three parameters: the maximum bridging stress, σ_{max}, the crack width at σ_{max}, w_{max}, and the crack width when bridging stress becomes to zero, w_{tu}. The values of σ_{max} and w_{max} of the model can be obtained directly from the calculation results. The value of w_{tu} is determined to have an equivalent fracture energy with the calculated bridging law in the softening branch. The modeled bridging laws for each fiber orientation intensity k are shown in **Figure A.5**. The comparison between the calculated bridging laws and the models in $k = 0.1$, 1, 10 are also shown in **Figure A.6**.

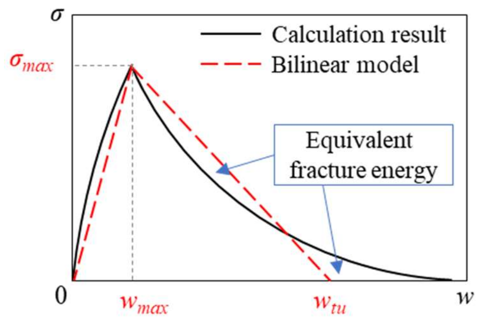

Figure A.4 Bilinear model for bridging law

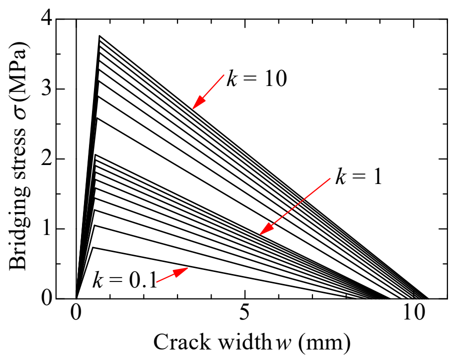

Figure A.5 Modeled Bridging laws

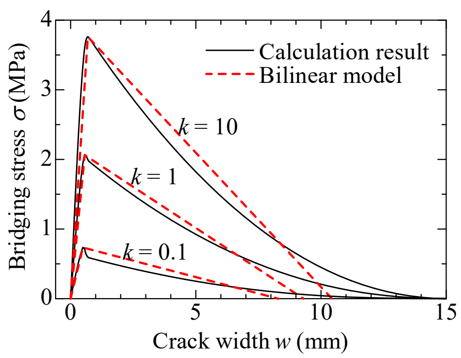

Figure A.6 Comparison between the calculated bridging laws and models

The three parameters in the model are expressed as a function of the fiber orientation intensity k to simplify the modeling of bridging law. The relationships between the parameters and k are shown in **Figure A.7**. The dotted lines in all figures exhibit the regression calculation results by the least square method. The solid lines exhibit the modified regression calculation result to simplify the relational expression between each parameter and k as given by Eq.(A.2) to Eq.(A.4).

$$\sigma_{max} = 2.0k^{0.3} \text{ (MPa)} \tag{A.2}$$

$$w_{max} = 0.60k^{0.07} \text{ (mm)} \tag{A.3}$$

$$w_{tu} = 9.3k^{0.05} \text{ (mm)} \tag{A.4}$$

The characteristic points of bilinear model of bridging law (**Figure A.4**) in each fiber orientation intensity k can be easily obtained by using these equations.

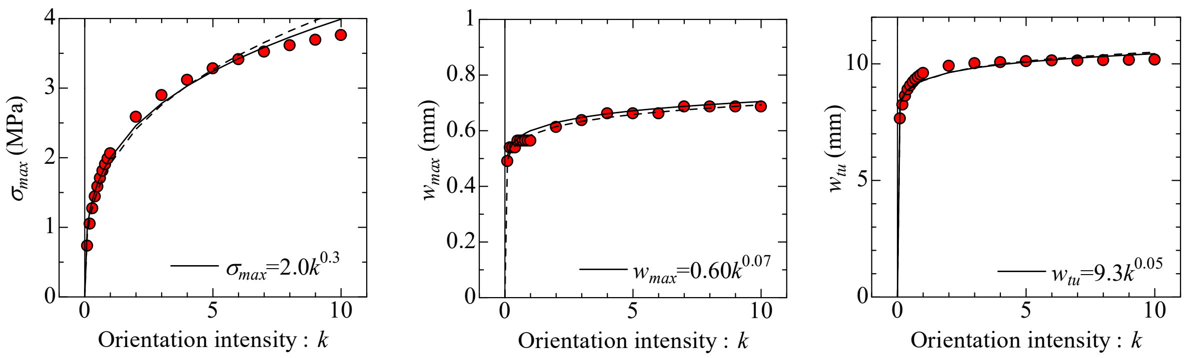

(a) (b) (c)

Figure A.7 Relationship between each parameter of model and orientation intensity k: (a) σ_{max} – k relationship; (b) w_{max} – k relationship; (c) w_{tu} – k relationship

References

[1] Matsumoto, T., Mihashi, H., (2002), "JCI-DFRCC Summary Report on DFRCC Terminologies and Application Concepts", Proceedings of the JCI International Workshop on Ductile Fiber Reinforced Cementitious Composites (DFRCC), pp.59-66.

[2] Rokugo, K., Kanda, T. eds., (2013), "Strain Hardening Cement Composites: Structural Design and Performance", RILEM State-of-the-Art Reports 6, 90pp.

[3] Li, V.C., (2019), "Engineered Cementitious Composites (ECC) - Bendable Concrete for Sustainable and Resilient Infrastructure", Springer: Germany, 419pp.

[4] Löfgren, I., (2005), "Fiber-Reinforced Concrete for Industrial Construction – A Fracture Mechanics Approach to Material Testing and Structural Analysis," PhD thesis, Department of Civil and Environmental Engineering, Chalmers University of Technology, Gothenburg, Sweden.

[5] Balaguru, P. N., Shah, S. P., (1992), "Basic Concepts and Mechanical Properties: Tension", Fiber-Reinforced Cement Composites, McGraw-Hill, New York, NY, USA, pp.37-84.

[6] Amin, A., Foster, S. J., Muttoni, A., (2015), "Derivation of the σ-w Relationship for SFRC from Prism Bending Tests", Structural Concrete, Vol. 16, Issue 1, pp.93-105.

[7] Eduardo B. Pereira, Gregor Fischer, Joaquim A. O. Barros., (2012), "Direct assessment of tensile stress-crack opening behavior of Strain Hardening Cementitious Composites (SHCC)", Cement and Concrete Research, Vol. 42, Issue 6, pp.834-846.

[8] Jing Yu, Christopher K. Y. Leung, (2018), "Novel experimental method to determine crack-bridging constitutive relationship of SHCC using digital image processing", Strain-Hardening Cement-Based Composites SHCC-4, Springer, Dresden, Germany, Vol. 15, pp.55-62.

[9] Li, V.C., (1993), "Micromechanics of Crack Bridging in Fibre-Reinforced Concrete", Material and Structures 26, pp.486-494

[10] Laranjeira, F., (2010), "Design-oriented Constitutive Model for Steel Fiber Reinforced Concrete", PhD-thesis. Universitat Politècnica de Catalunya, Spain.

[11] En-Hua Yang, Shuxin Wang, Yingzi Yang and Victor C. Li, (2008), "Fiber-Bridging Constitutive Law of Engineered Cementitious Composites", Journal of Advanced Concrete Technology, Vol. 6, No. 1, pp.181-193.

[12] Kanakubo, T., Miyaguchi, M., Asano, K., (2016), "Influence of Fiber Orientation on Bridging Performance of Polyvinyl Alcohol Fiber-Reinforced Cementitious Composite", Materials Journal, American Concrete Institute, Vol.113, No.2, pp.131-141.

[13] Kanakubo, T., Echizen, S., Wang, J., Mu, Y., (2020), "Pullout Behavior of Bundled Aramid Fiber in Fiber-Reinforced Cementitious Composite", Materials 2020, 13(7), 1746.

[14] Ozu, Y., Miyaguchi, M. Kanakubo, T., (2018), "Modeling of Bridging Law for PVA Fiber-Reinforced Cementitious Composites Considering Fiber Orientation." Journal of Civil Engineering and Architecture 12, 651-661

[15] Kanakubo, T., Yamato, N., (2014), "Crack Width Prediction Method for Steel and FRP Reinforcement Based on Bond Theory." Journal of Advanced Concrete Technology Vol.12, pp.310-319

[16] Deluce J., Lee S.C., (2012), Vecchio F.J., "Crack Formation in FRC Structural Elements Containing Conventional Reinforcement", In: Parra-Montesinos G.J., Reinhardt H.W., Naaman A.E. (eds) High Performance Fiber Reinforced Cement Composites 6, RILEM State of the Art Reports, vol 2, Springer, Dordrecht, pp.271-278.

[17] Kunieda, M., Hussein, M., Ueda, N and Nakamura, H., (2010), "Enhancement of crack distribution of UHP-SHCC under axial tension using steel reinforcement." J. of Advanced Concrete Technology, 8(1), pp.49-57

[18] Fischer, G., Li, V.C., (2002), "Influence of Matrix Ductility on Tension-Stiffening Behavior of Steel Reinforced Engineered Cementitious Composites (ECC)", Structural Journal, American Concrete Institute, Vol.99, No.1, pp.104-111.

[19] Stang, H., Aarre, T., (1992), "Evaluation of Crack Width in FRC with Conventional Reinforcement", Cement and Concrete Composites 14, pp.143-154.

[20] Amin, A., Gilbert, R. I., (2018), "Instantaneous Crack Width Calculation for Steel Fiber-Reinforced Concrete Flexural Members", Structural Journal, American Concrete Institute, Vol.115, No.2, pp.535-543.

[21] Ogura, H., Kunieda, M., Nakamura, H., (2019), "Tensile Fracture Analysis of Fiber Reinforced Cement-Based Composites with Rebar Focusing on the Contribution of Bridging Forces", Journal of Advanced Concrete Technology Vol.17, 216-231

[22] Sunaga, D., Kanakubo, T., Namiki, K., (2019), "Study on Evaluation of Crack Width in Steel Reinforced DFRCC Members", Proceedings of the Japan Concrete Institute, Vol.41, No.2, pp.1171-1176. (in Japanese)

[23] Ozu, Y., Watanabe, K., Yasojima, A., Kanakubo, T., (2016), "Evaluation of Size Effect in Bending Characteristics of DFRCC Based on Bridging Law," ACF 2016, The 7th International Conference of Asian Concrete Federation, 3. Concrete structures, Paper No.32.

[24] Hashimoto, H., Mu, Y., Yamada, H., Kanakubo, T., (2017), "Slip-Out Characteristics of Aramid and PP Fibers and Calculation of Bridging Law", Concrete Research and Technology, Vol.28, pp.103-111. (in Japanese)

[25] Hashimoto, H., Yamada, H., Yasojima, A., Kanakubo, T., (2016), "Slip-Out Characteristics of Steel Wire and Calculation of Bridging Law", Proceedings of the Japan Concrete Institute, Vol.38, No.1, pp.249-254. (in Japanese)

[26] Asano, K., Kanakubo, T., (2016), "Study on Size Effect in Bond Splitting Behavior of ECC", Bond in Concrete 2012, Volume 2. Bond in New Materials and under Severe Conditions, pp.855-859

[27] Kanda, T., and Li, V. C., (1998), "Interface Property and Apparent Strength of High-Strength Hydrophilic Fiber in Cement Matrix", Journal of Materials in Civil engineering, ASCE, Vol.10, No.1, pp.5-13.